metals

Article

Numerical Simulation and Experimental Measurement of Residual Stresses in a Thick-Walled Buried-Arc Welded Pipe Structure

Mato Perić [1,*], Ivica Garašić [2], Nenad Gubeljak [3], Zdenko Tonković [2], Sandro Nižetić [4] and Krešimir Osman [5]

[1] Department of Mechanical Engineering, University North, 104 Brigade 3, 42000 Varaždin, Croatia
[2] Faculty of Mechanical Engineering and Naval Architecture, University of Zagreb, Ivana Lučića 5, 10000 Zagreb, Croatia; ivica.garasic@fsb.hr (I.G.); zdenko.tonkovic@fsb.hr (Z.T.)
[3] Faculty of Mechanical Engineering, University of Maribor, Smatanova Ulica 17, 2000 Maribor, Slovenia; nenad.gubeljak@um.si
[4] LTEF Laboratory of Thermodynamics and Energy Efficiency, Faculty of Electrical Engineering, Mechanical Engineering and Naval Architecture, University of Split, Ruđera Boškovića 32, 21000 Split, Croatia; snizetic@fesb.hr
[5] Department of Electrical Engineering, Zagreb University of Applied Sciences, Konavoska 2, 10000 Zagreb, Croatia; kresimir.osman@tvz.hr
* Correspondence: mato.peric@fsb.hr; Tel.: +385-1-3845-147

Abstract: In this study, a numerical simulation of a single pass welding of two thick-walled pipes with the buried-arc method was performed in order to determine the residual stresses caused by welding. The numerical simulation procedure in the thermal analysis was performed by the element birth and death method while the structural analysis was performed simultaneously, without the application of the element birth and death technique in order to reduce the duration of the numerical simulation. The simulation results were validated by experimental residual stress measurements on the outside surfaces of the welded model using the X-ray diffraction technique. A good agreement between the results of the numerical simulation and experimental measurements was confirmed.

Keywords: buried-arc welding; thick-walled pipe; single-pass welding; X-ray diffraction; submodeling; MAG welding

check for updates

Citation: Perić, M.; Garašić, I.; Gubeljak, N.; Tonković, Z.; Nižetić, S.; Osman, K. Numerical Simulation and Experimental Measurement of Residual Stresses in a Thick-Walled Buried-Arc Welded Pipe Structure. *Metals* **2022**, *12*, 1102. https://doi.org/10.3390/met12071102

Academic Editors: Tomasz Kik and Frank Czerwinski

Received: 24 May 2022
Accepted: 26 June 2022
Published: 28 June 2022

1. Introduction

Butt-welded pipes comprise the majority of welds in various industries such as the petrol and gas industry, shipbuilding, chemical and thermal power plants, etc. Traditionally, due to the low cost of metal active gas (MAG) technology and the ease of its use, it is a very widespread pipe welding process for large wide diameter ranges and wall thicknesses. This process is characterized by the high local input of heat required to melt the electrode which is then rapidly transferred to the base material of the structure. The subsequent rapid cooling of molten materials leads to material shrinkage in the weld zone and its immediate vicinity. It is generally known that this phenomenon leads to the appearance of undesirable effects such as changes in the crystal structure, changes of mechanical properties in the weld zone and the occurrence of permanent plastic deformations and residual stresses [1–4]. Plastic deformations disrupt the external appearance and cause dimensional deviations which is a problem when assembling pipe structures, while on the other hand, residual stresses contribute to the appearance of cracks and generally shorten the life of the welded structure [5,6]. Although there are effective thermal [7,8] and mechanical [9,10] procedures for the removal of residual stresses and plastic deformations in engineering practice, their application is often limited by the size of the structure, large number of welds, operating conditions and additional financial costs. Nowadays, the magnitude of residual stresses and strains can be predicted using numerical simulations, i.e., preventive measures should already be taken to reduce them in the design phase, thus avoiding the cost of subsequent repairs [11–14]. These methods primarily include an adequate choice of weld shapes and dimensions, welding sequences, number of passes, heat input and mechanical boundary conditions. In doing so, Teng and Chang [15] were among the first to perform a numerical simulation of two butt-welded pipes of very small wall thickness by using a two-dimensional sequential model. The conducted research provided insight into the temperature distribution during welding as well as the final state of residual stresses. Here, the numerical results obtained were not verified experimentally, but their value was shown in a number of studies that followed later. Due to the attractiveness of the topic, residual stresses in MAG butt-welded pipes have been the subject of research in numerous numerical and experimental studies in the last thirty years. Deng and Murakawa [16] developed a numerical procedure based on the ABAQUS code to simulate a temperature field, residual stress field and phase transformations for the case of multipass welding for two 2.25Cr-1Mo steel pipes. The residual stresses measured by the blind hole-drilling technique of stress relaxation showed good agreement with the numerical calculation. Giri et al. [17] presented research on the effect of weld groove on residual stresses in thick steel pipes used by boiling water systems and steam pipes. They conducted experimental measurements of residual stresses with the blind hole-drilling technique with an accompanying numerical simulation. The obtained numerical results agreed well with the experimental ones. Zhao et al. [18], on the example of thick-walled steel pipes with a large diameter, investigated the distribution of temperatures during welding as well as the influence of temperature fields on the microstructure of the weld metal. The numerically predicted hardness, microstructure and phase composition confirmed good correlation with the results of experimental measurements. Wu et al. [19] numerically and experimentally investigated the bending deformations caused by MAG welding on the example of butt-welded pipes. Liu et al. [20] used a combined shell/3D model in research of a temperature field and residual stresses. The obtained results were in good correlation with the full 3D model as well as experimental measurements.

From the above cited references, it is evident that all pipe models were welded using a conventional MAG technique, which in the case of welding thick pipes requires many electrode passes to fill the weld groove. This reduces production efficiency and the manufacturing process itself is unnecessarily prolonged, which is a significant disadvantage of the conventional MAG process. Therefore, for the needs of the industry, an improved MAG process was developed (in the literature also known as buried-arc welding), characterized by higher welding currents and voltage, higher speeds of welding wire supplies and deeper weld penetrations. This technique enables the butt-weld welding of structures up to approximately 30 mm in thickness in one pass. Compared to the conventional MAG process, the buried-arc process is also characterized by a smaller volume of weld grooves, which saves filler material. In addition, due to the reduced number of weld passes, the consumption of electricity is lower as well as the consumption of shielding gas.

It can be concluded that unlike the conventional MAG procedure, the study of residual stresses and strains in the scientific and professional literature for the case of buried-arc welded structures are very rare. In the authors' earlier works, numerical and experimental welding was performed on the examples of butt-welded plates [21], T-joint welded plates [22] and a circular disk model [23]. In this paper the research of residual stresses was extended to thick steel pipes welded with the buried-arc procedure, which according to the authors' knowledge is the first in the literature.

The paper consists of five sections. A brief description of buried-arc welding technology is given in Section 2. Section 3 describes the applied experimental model. Within Section 4, a detailed description of the numerical welding simulation model is given. Section 5 presents the results of numerical simulations compared to experimental measurements. The final conclusions of the paper are provided in the last section.

2. Buried-Arc Welding Technology in Brief

For the welding of thick structures, processes such as submerged arc welding [24], electroslag welding [25] and electrogas arc welding [26] have been applied in industrial production. Nowadays, laser hybrid welding processes [27] are also well known and used along with plasma arc welding [28], especially with "keyhole" technology and in some special cases electron beam welding [29]. However, conventional MAG welding is more flexible and applicable in conventional metal transfer modes, but in areas of high currents, when unstable arc and intensive spattering can occur if the arc control is not at the highest level.

This leads to the development of a new welding process based on MAG called "buried arc". What is specific for this process is the fact that the arc is generated at a lower position under the surface of the molten pool and the space around it is the liquid metal of the molten pool. The metal transfer in this process is in the "buried" cavity which is supported by the pressure of the arc plasma. To support this kind of arc phenomena, a high current range above 500 A is required, together with a unique high speed wire feed system with a wire buffer. Furthermore, the welding power source, which consists of two digital inverter-controlled units, is necessary to obtain enough current and enable the physics of the process. The buried arc space is very unstable as the geometry of the cavity is changed due to the welding current and instantaneous arc voltage variations. The metal transfer consists of a droplet transfer and rotating arc and the conditions for stable welding are within a very narrow range. Therefore, a precise and fast control of the process is of importance to achieve an applicable process. For a more detailed description of the buried-arc welding technology, readers are referred to [30].

3. Experimental Investigations

Two pipes made of non-alloyed carbon steel S355J2+N steel and dimensions Ø168 × 12 mm, without pipe-end preparation, were buried-arc welded by using a seven-axis robot (Figures 1 and 2). The welding was performed in ISO 6947: PA position. Pipe rotation with constant speed was applied to achieve the required welding velocity. The electrode inclination angle was neutral. In order to maintain I-bevel preparation, tack welds were made from the inner side on metallic backing plates with a 120° disposition. With this solution, full penetration weld could be done in a single pass. The pipe was fixed with a clamping head from one side and a rotary positioner was applied from the other side of the sample to enable rotation without eccentric movements (Figure 1). A return current path was connected through the clamping head sliding contacts. For welding, a wire A: G 42 4 C/M G3Si1 with a diameter of 1.6 mm in accordance with the ISO 14341 standard was selected. During welding, the metal transfer was stable and without significant interruptions or spattering. The main welding parameters used in this experiment are given in Table 1. Upon completion of welding, the quality of the weld was inspected visually in accordance with the ISO 17637 standard, and no surface imperfections were found.

Figure 1. Pipes prepared for welding.

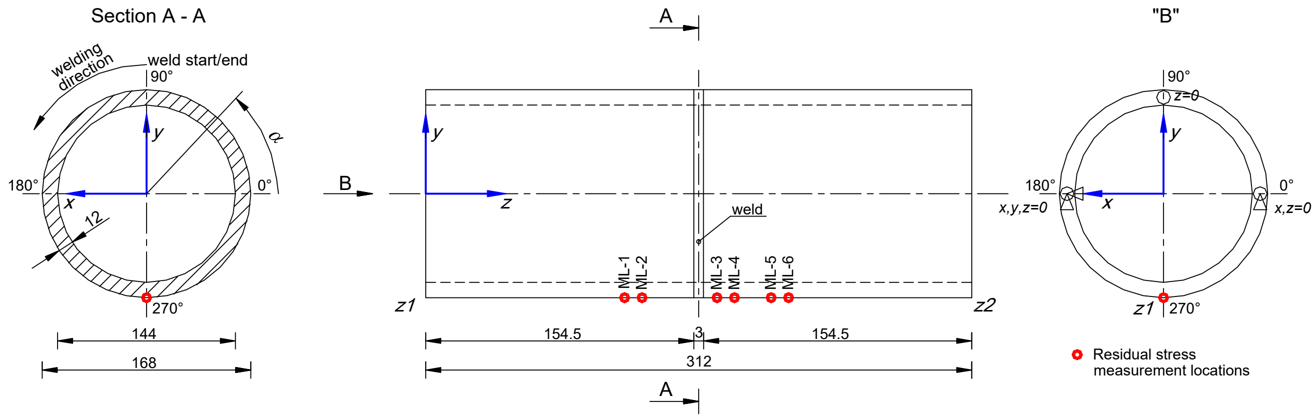

Figure 2. Geometry and dimensions of welded pipes (dimensions in millimeters).

Table 1. Main welding parameters.

Welding Current I	Welding Voltage U	Wire Diameter	Welding Time Duration	Shielding Gas Composition	Shielding Gas Flow
540 A	40 V	1.6 mm	68 s	100 CO_2	25 L/min

After welding and cooling the sample to ambient temperature, by using the X-ray diffraction cosα-method [31] using the Pulstec μ-X360 device (Pulstec Industrial Co., Ltd., Shizuoka, Japan), the residual stresses were measured. The measurement of residual stresses on the outer surface of the pipe (line $z1$-$z2$, α = 270°, Figure 2) was performed at six locations labeled ML-1 (z = 115 mm), ML-2 (z = 124 mm), ML-3 (z = 167 mm), ML-4 (z = 177 mm), ML-5 (z = 197 mm) and ML-6 (z = 208 mm). Prior to the start of the measurement, the measurement locations were electropolished and the measurement was performed at a depth of 0.015 mm below the upper surface of the pipe. Electropolishing was performed by using the EP-3 device, also a product of Pulstec Industrial Co. Ltd. The experimental setup for measuring welding residual stresses with the X-ray method is shown in Figure 3.

Figure 3. X-ray residual stress measurement.

4. Welding Numerical Simulation

The numerical simulation of the welding process was performed by a sequential procedure consisting essentially of two steps. In the first step, a nonlinear heat transfer analysis was performed to obtain the spatio-temporal distribution of temperatures in each time increment. In the second step, the obtained temperature distribution was used as the heat load in the structural analysis. In both analyses, the temperature-dependent thermal and mechanical properties of the materials were applied and are given in Figures 4 and 5, while its chemical composition is provided in Table 2.

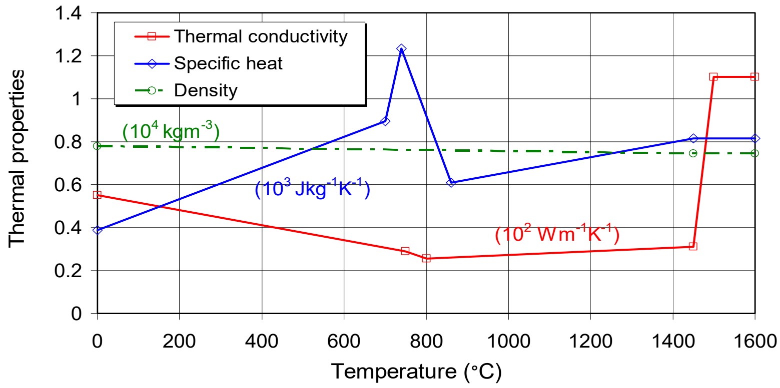

Figure 4. S355J2+N steel, thermal properties [32].

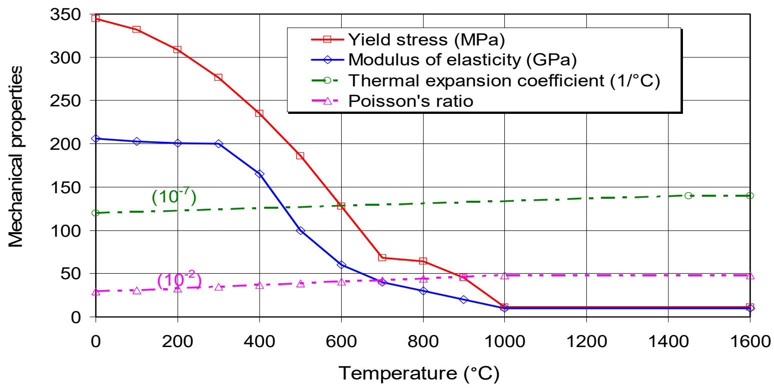

Figure 5. S355J2+N steel, mechanical properties [32].

Table 2. Chemical composition of S355J2+N steel (mass%), [23].

C	Si	Mn	P	S	N	Cu	Cr	Ni	Mo	Al	V	Ti	Nb
0.17	0.24	1.25	0.016	0.006	0.008	0.23	0.06	0.1	0.11	0.0032	0.005	0.025	0.033

In the thermal numerical simulation, the space-time temperature field distribution was obtained by solving non-linear differential Equation (1) that is derived from Fourier's law of heat conduction and law of energy conservation:

$$k(\frac{\partial^2 T}{\partial x^2} + \frac{\partial^2 T}{\partial y^2} + \frac{\partial^2 T}{\partial z^2}) + Q = \rho C \frac{\partial T}{\partial t} \quad (1)$$

In Equation (1), k, ϱ and C represent thermal conductivity, density and specific heat capacity, respectively, T is the temperature, while Q represents the external heat introduced to the welded specimen which can be expressed in the form:

$$Q = \frac{\eta UI}{V_H} \quad (2)$$

In Equation (2), η, U and I represent welding process efficiency, voltage and current, respectively, while V_H denotes the volume of the activated set of finite elements of the weld bead. In this study, a value of 85% was taken for the efficiency of the welding process. The following boundary conditions necessary for the solution of Equation (1) on the external surfaces of the welded pipes were assumed: the temperature-independent convective heat transfer coefficient (h_c = 10 $\mathrm{Wm^{-2}K^{-1}}$) and emissivity (ε = 0.9). The element birth and death technique was applied to simulate the movement of the electrode and weld filler addition. For this purpose, the entire 3 mm wide and 12 mm thick weld ring was divided into 68 sets of finite elements. All 68 sets of finite elements representing the volume of the weld were virtually removed in the first step of the numerical simulation (element death). In the following step, individual sets of finite elements (element birth) were reactivated with applied heat flux of $Q = 7.08 \times 10^{10}$ $\mathrm{Jm^{-3}s^{-1}}$ to each individual set of finite elements. Here, a pure volumetric heat flux with uniformly distributed heat input per weld volume was applied [33]. Thus, the activation of the finite element sets simulated the movement of the welding torch and filler metal addition. It is important to note that each of the 68 element sets in the numerical simulation was first added (reactivated) in a very short time interval, e.g., 10^{-7} s, and then subjected for 1 s to heat flux. Adding the 68th set of finite elements, the welding process ended and started the 8500-s cooling process. In the thermal analysis, DC3D8 three-dimensional eight-node linear hexahedral finite elements with full integration were used.

In order to reduce the duration of the simulation, the structural analysis was performed in one step, also without the application of the birth and death technique [34]. Here, base metals and weld fillers were considered as full isotropic and elastic-perfect plastic metals that yield in accordance with the von Mises criterion and the associated flow rule [35,36]. In the numerical simulation, due to the lack of accurate thermal and mechanical data for the weld filler, its properties were considered identical to the base material. Due to the very short exposure of the material to high temperatures, creep material was not taken into account. Furthermore, phase transformations of materials due to the low impact on the post-weld residual stress field in the case of welding structures made of carbon steel were neglected [37–39]. Taking into account these simplifications, the total strain tensor can be expressed in the form:

$$d\varepsilon^{total} = \{d\varepsilon^{e}\} + \{d\varepsilon^{p}\} + \left\{d\varepsilon^{th}\right\} \tag{3}$$

In the structural simulation, C3D8I finite elements with incompatible nodes were used and the complete sequential procedure of the numerical welding simulation was presented in the authors' previous study [40]. The finite element mesh consisted of 42,432 elements and is shown in Figure 6. For better visibility, only half of the global model and submodel are shown.

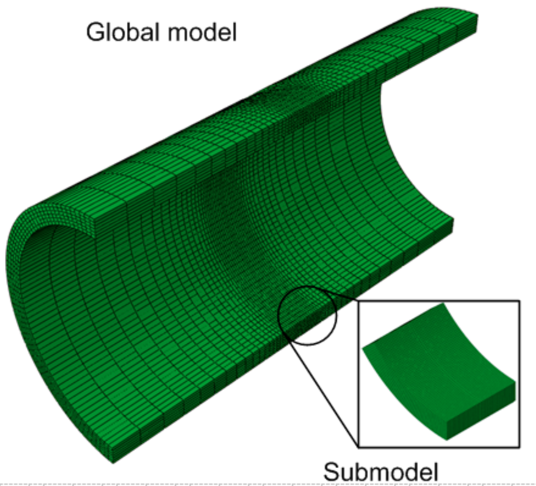

Figure 6. Finite element mesh of welded pipes.

It can be seen that a denser mesh was used in the weld zone where the temperature and stress gradients are very high. Mesh convergence was checked using the global-local submodeling technique [41]. In both the thermal and mechanical analyses, the same finite element mesh was used, only with the conversion of DC3D8 elements from the thermal analysis to C3D8I ones in the structural analysis. The mechanical boundary conditions used in this study are shown in Figure 2. Both numerical simulations were performed by using the ABAQUS software (version 6.14, ABAQUS Inc., Palo Alto, CA, USA).

5. Results and Discussion

A comparison of the axial and hoop residual stress distributions of the global model and submodel along line $z1$-$z2$, α = 90°, (Figure 2), is given in Figure 7. The full-field comparison of the global model and submodel is shown in Figure 8. Here it can be seen that the stresses of the global model and submodel match very well, which means that the global model mesh was well designed.

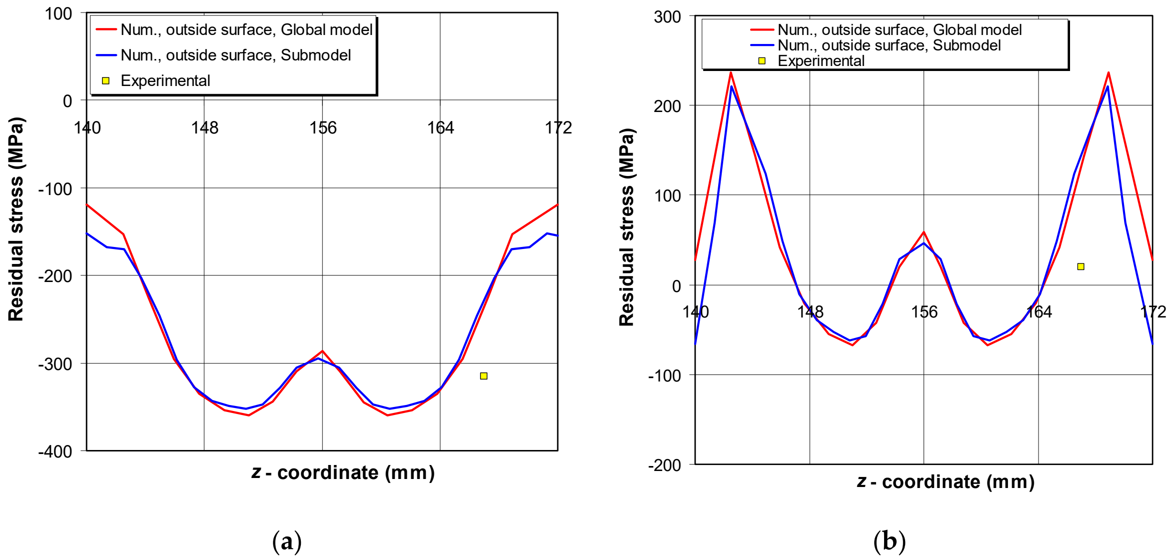

Figure 7. Residual stress profiles of global model and submodel along line $z1$-$z2$, α = 90°, (Figure 2), (**a**) axial stress, (**b**) hoop stress.

Temperature histories for three randomly selected nodes 15 mm away from the weld centerline (outside surface, z = 141 mm, α = 180°, α = 270° and α = 0°, Figure 2) are shown in Figure 9. It can be seen that the peak temperatures reach the value of 625 °C and that the temperature profile remains stationary and independent at an α angle. The exception to the stationary profile is only near the start/end point of welding. As mentioned in the previous section, the obtained temperature field is the load in the structural analysis, thus the stationarity of the temperature field is directly reflected in the residual stress field. Figure 10 shows the moving of the electrode and the peak process temperature of 3929 °C, resulting from the very high welding current and voltage of the buried-arc process, i.e., large heat input per weld volume. Furthermore, the reason for such a numerically obtained high temperature in the weld pool lies in the neglect of coupling between the solid and liquid phase. This phenomenon is not directly embedded in the ABAQUS software, which can lead to unrealistically high temperatures within the weld pool and is significantly different from the realistic situation. This problem can be partially alleviated by artificially increasing the thermal conductivity at temperatures above the melting point [37]. As the area of extremely high temperatures covers a very small volume of the weld and as this is a single-pass weld, this phenomenon has little impact on post-weld residual stresses and deformations.

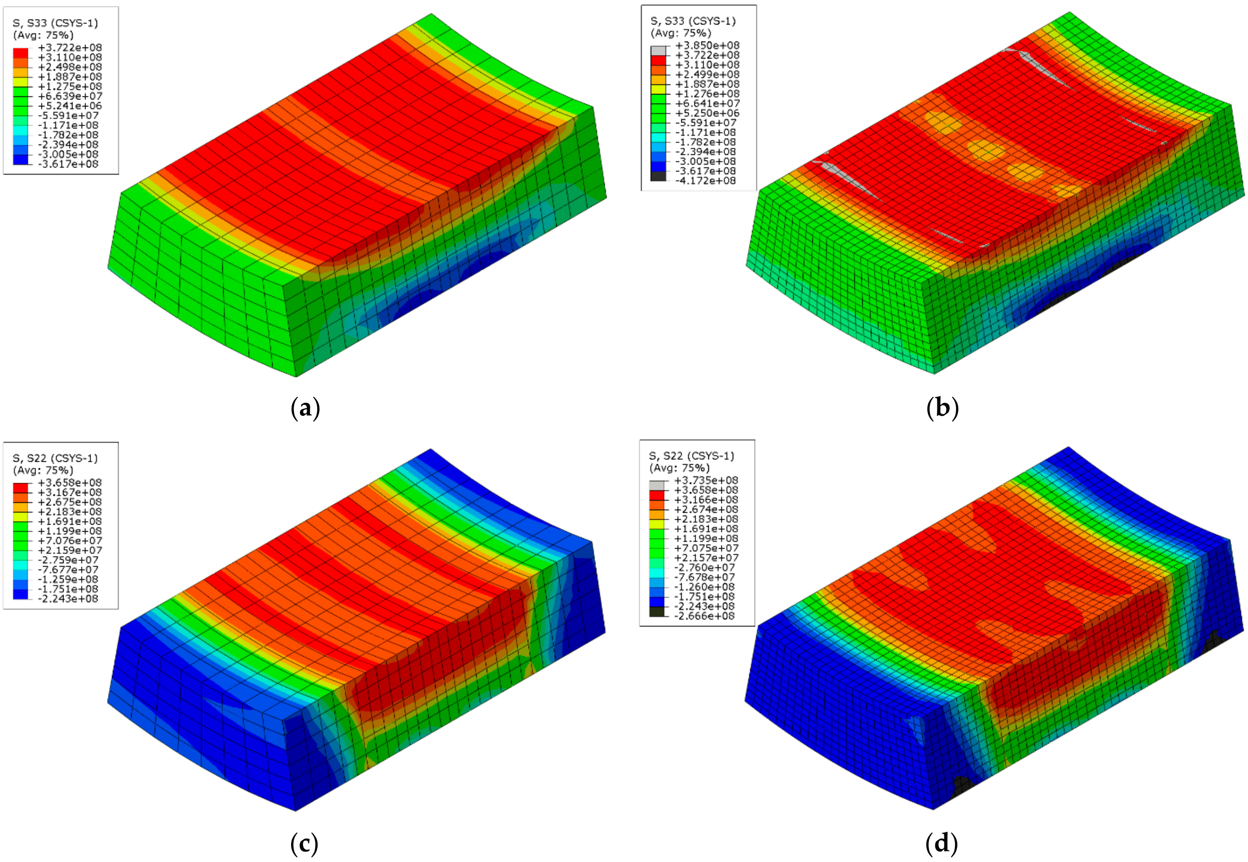

Figure 8. Full field residual stress distribution; (**a**) axial residual stress—global model, (**b**) axial residual stress—submodel, (**c**) hoop residual stress—global model, (**d**) hoop residual stress—submodel.

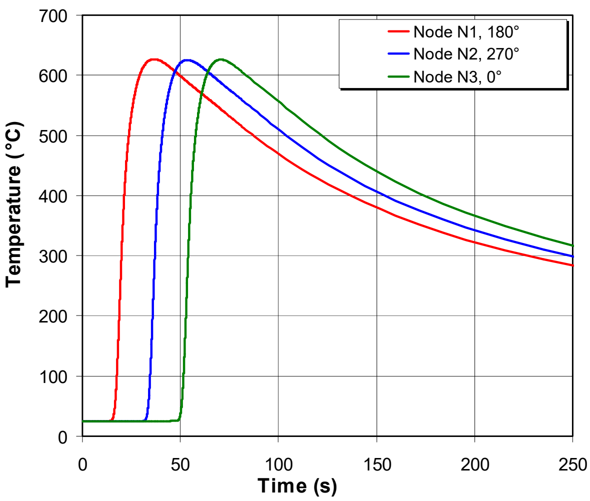

Figure 9. Temperature histories at three nodes (outside surface, z = 141 mm, α = 180°, α = 270° and α = 0°).

Figure 11 shows the axial stress distributions along line $z1$-$z2$, α = 270° (Figure 2) on the outside surface of welded pipes with the results of X-ray measurements. The numerically obtained axial residual stresses are compressive in the weld and its vicinity, reaching a minimum value of −360 MPa at a distance of 5 mm from the weld centerline. The maximum tensile stress is 79 MPa at a distance of 51 mm from the weld centerline. It can be confirmed that the numerically calculated results of axial stresses are in good correlation with the experimentally obtained ones. In Figure 12, the axial stress distributions along line $z1$-$z2$,

$\alpha = 270°$ (Figure 2) on the inside surface of the welded model is presented. It can be seen that unlike the outside surface, tensile residual stresses dominate here and reach a value of 372 MPa, while the minimum compressive stress reach −82 MPa.

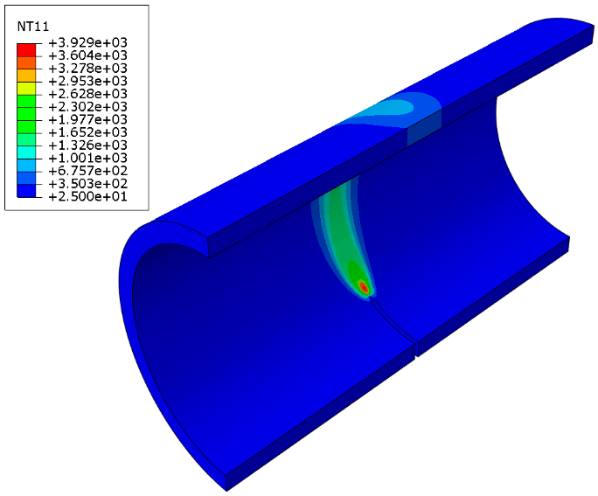

Figure 10. Peak process temperature and moving the electrode.

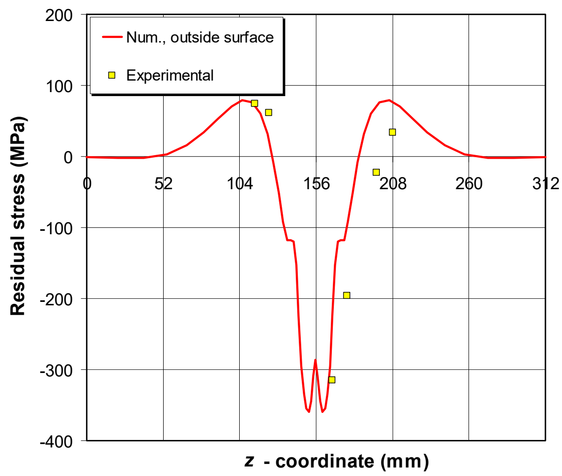

Figure 11. Axial residual stress distribution on outside surface of welded pipes along line *z*1-*z*2 (Figure 2), $\alpha = 270°$.

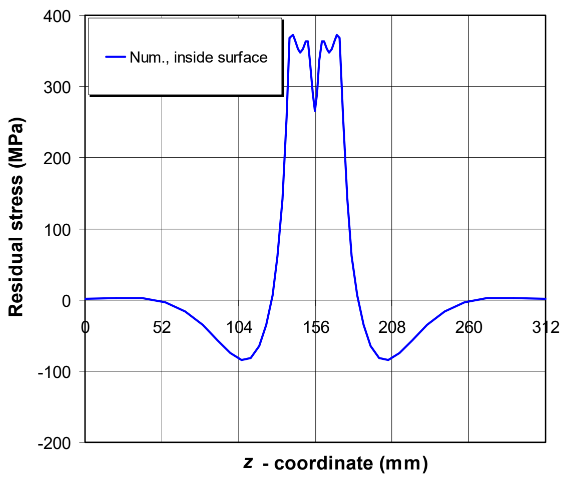

Figure 12. Axial residual stress distribution on inside surface of welded pipes along line *z*1-*z*2 (Figure 2), $\alpha = 270°$.

Figure 13 shows hoop stress distributions along line $z1$-$z2$, α = 270° (Figure 2) on the outside surface of the welded model and it can be noticed that the stress distribution is very uneven here. This phenomenon was also observed in previous research on welded thin pipes [42]. Very sudden changes in stresses are also reflected in differences compared to experimental measurements. The amplitude range of hoop stresses is between −221 and 236 MPa. In contrast, residual stress hoop distribution on the inner side (Figure 14) is steady in a range of −177 to 335 MPa. Generally speaking, axial and hoop stresses exist only in the weld and zones close to it, while towards the ends of the pipe they disappear.

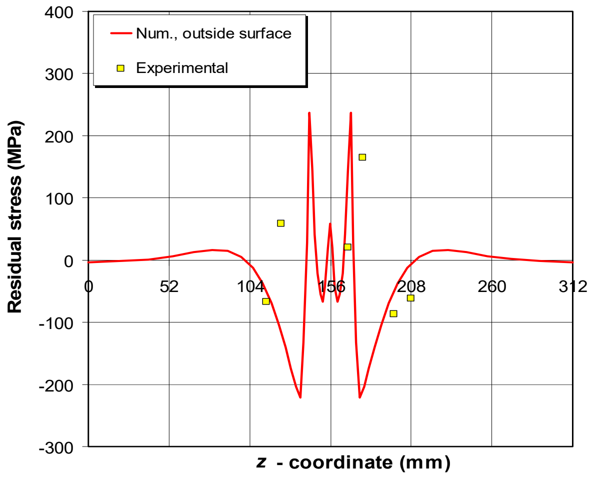

Figure 13. Hoop residual stress distribution on outside surface of welded pipes along line $z1$-$z2$ (Figure 2), α = 270°.

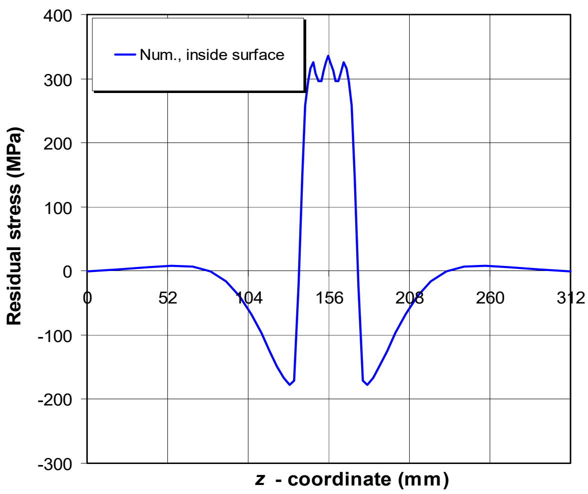

Figure 14. Hoop residual stress distribution on inside surface of welded pipes along line $z1$-$z2$ (Figure 2), α = 270°.

Axial and hoop residual stress distributions through the pipe thickness are shown in Figure 15. If the areas close to the outer and inner surface are neglected, it can be noticed that the change of axial residual stresses from tensile to compressive is almost linear and almost symmetrical with respect to the middle pipe surface, while hoop stresses always remain positive. Cross sections through thickness axial and hoop residual stress distributions (z = 156 mm, Section A-A, Figure 2) are shown in Figures 16 and 17, respectively. Figures 18 and 19 show full field axial and hoop stress distributions, respectively, and for better visibility only the left half of the welded model (Figure 2) is shown.

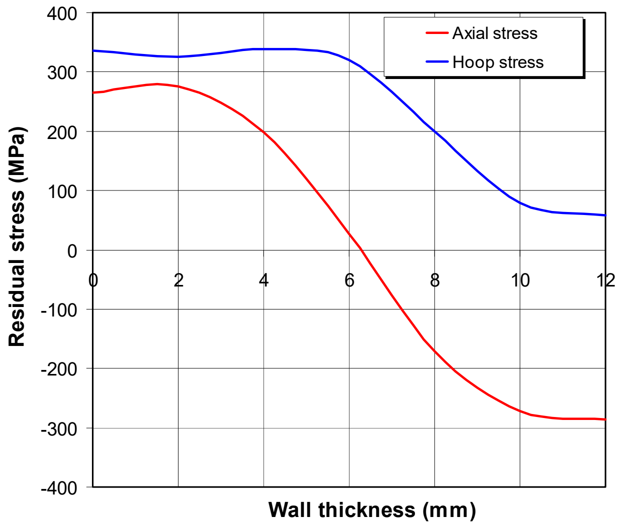

Figure 15. Axial and hoop residual stress distribution through pipe thickness (z = 156 mm, α = 270°, Figure 2).

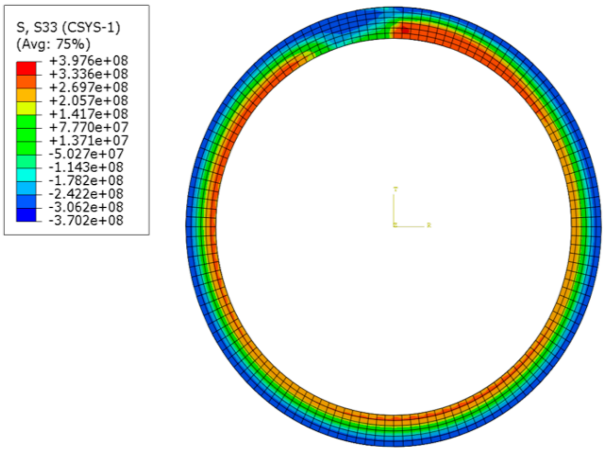

Figure 16. Cross section axial residual stress distribution (distributions (z = 156 mm, Section A-A, Figure 2).

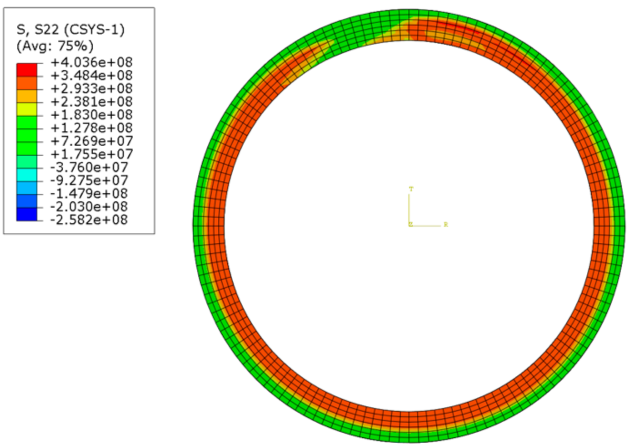

Figure 17. Cross section hoop residual stress distribution (distributions (z = 156 mm, Section A-A, Figure 2).

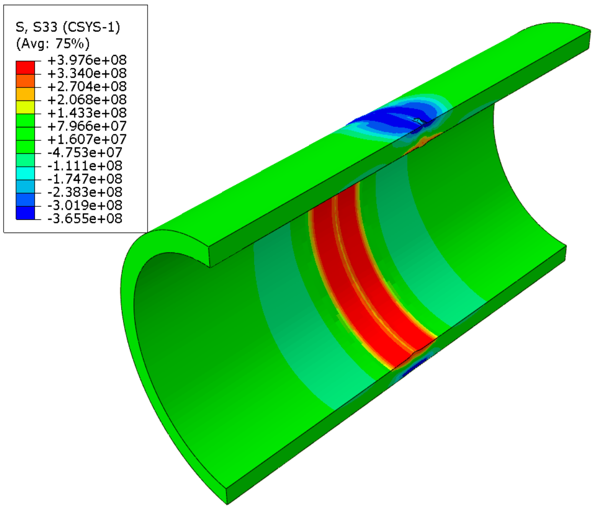

Figure 18. Full-field axial residual stress distributions.

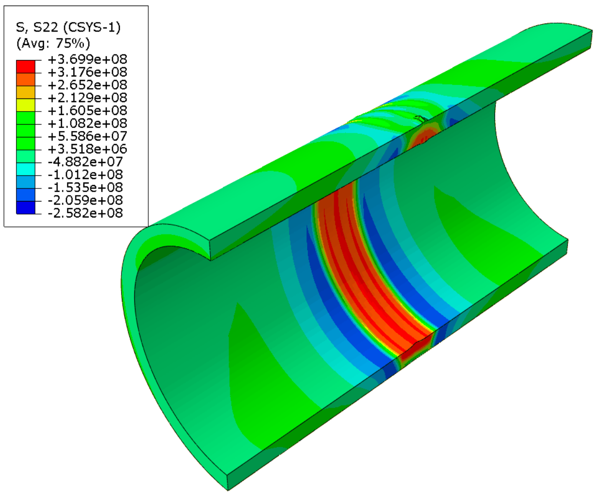

Figure 19. Full-field hoop residual stress distributions.

6. Conclusions

In the frame of this numerical and experimental study, investigations of the temperature field during welding as well as post-weld residual stresses for the case of a single-pass welding of two thick pipes made of non-alloyed S355 carbon steel by using the buried-arc technique were conducted, which according to the authors' knowledge is the first case in the scientific and professional literature. The conclusions are as follows:

- Temperature histories after the start of welding become steady very quickly along the welding path.
- Axial residual stress at the weld centerline on the outer surface are compressive. As they move away from the welds, they become tensile and disappear towards the ends of the pipe. The comparison of numerically and experimentally obtained stresses showed very good agreement.
- Axial residual stress at the weld centerline on the outside surface are tensile. As they move away from the welds, they become compressive and disappear towards the ends of the pipe.
- Hoop stresses on the outer surface of welded pipes very quickly change the sign of stress and disappear towards the ends of the pipe. The deviation in the measured and numerically calculated results is greater compared to axial residual stresses due to sudden changes in hoop stresses in the weld zone.

- Hoop stresses on the inner surface of welded pipes in the weld zone are tensile and as they move away from the welds become pressured and disappear towards the ends of the pipe.
- Through the thickness change of residual stresses from compressive to tensile, it is almost linear if the effects at the outer or inner surface of the welded model are neglected.
- Hoop stresses through the thickness are always tensile.

Author Contributions: Conceptualization, M.P.; formal analysis, M.P.; writing—original draft preparation, M.P.; data curation, M.P., I.G. and K.O.; project administration, M.P., Z.T., S.N. and N.G.; experimental measurements, N.G., funding acquisition, Z.T. and I.G.; supervision, M.P., I.G., N.G., Z.T., S.N. and K.O. All authors have read and agreed to the published version of the manuscript.

Funding: This work has been supported by the European Union through the European Regional Development Fund, Operational Programme "Competitiveness and Cohesion" 2014–2020 of the Republic of Croatia, project "Improvement of high-efficiency welding technology" (ImproWE, KK.01.1.1.07.0076). The authors are grateful also for the residual stress equipment support from the Slovenia Research Agency in frame of Funding Programme P2-0137 "Numerical and Experimental Analysis Mechanical Systems".

Data Availability Statement: Not applicable.

Conflicts of Interest: The authors declare no conflict of interest.

References

1. Ghafouri, M.; Ahola, A.; Ahn, J.; Björk, T. Welding-induced stresses and distortion in high-strength steel T-joints. *J. Constr. Steel Res.* **2022**, *189*, 107088. [CrossRef]
2. Hirohata, M.; Nozawa, S.; Tokumaru, Y. Verification of FEM simulation by using shell elements for fillet welding process. *Int. J. Interact. Des. Manuf.* 2022, *in press*. [CrossRef]
3. Cai, S.; Zhang, Y.; Wu, J.; Wu, F. A fuzzy finite element model based on the eigenstrain method to evaluate the welding distortion of T-joint fillet welded structures. *J. Manuf. Process.* **2022**, *77*, 451–462. [CrossRef]
4. Kik, T.; Moravec, J.; Švec, M. Experiments and Numerical Simulations of the Annealing Temperature Influence on the Residual Stresses Level in S700MC Steel Welded Elements. *Materials* **2020**, *13*, 5289. [CrossRef] [PubMed]
5. Zhang, W.; Jiang, W.; Zhao, X.; Tu, S.T. Fatigue life of a dissimilar welded joint considering the weld residual stress: Experimental and finite element simulation. *Int. J. Fatigue* **2018**, *109*, 182–190. [CrossRef]
6. Xin, H.; Correia, J.A.F.O.; Veljkovic, M.; Berto, F.; Manuel, L. Residual stress effects on fatigue life prediction using hardness measurements for butt-welded joints made of high strength steels. *Int. J. Fatigue* **2021**, *147*, 106175. [CrossRef]
7. Gao, H.; Wu, S.; Wu, Q.; Li, B.; Gao, Z.; Zhang, Y.; Mo, S. Experimental and Simulation Investigation on Thermal-Vibratory Stress Relief Process for 7075 Aluminium Alloy. *Mater. Des.* **2020**, *195*, 108954. [CrossRef]
8. Song, H.; Gao, H.; Wu, Q.; Zhang, Y. Residual stress relief mechanisms of 2219 Al–Cu alloy by thermal stress relief method. *Rev. Adv. Mater. Sci.* **2022**, *61*, 102–116. [CrossRef]
9. Yang, Y.P. Understanding of Vibration Stress Relief with Computation Modeling. *J. Mater. Eng. Perform.* **2009**, *18*, 856–862. [CrossRef]
10. Gao, H.-J.; Zhang, Y.-D.; Wu, Q.; Song, J. Experimental Investigation on the Fatigue Life of Ti-6Al-4V Treated by Vibratory Stress Relief. *Metals* **2017**, *7*, 158. [CrossRef]
11. Sepe, R.; Greco, A.; De Luca, A.; Caputo, F.; Berto, F. Influence of thermo-mechanical material properties on the structural response of a welded butt-joint by FEM simulation and experimental tests. *Forces Mech.* **2021**, *4*, 100018. [CrossRef]
12. Lorza, R.L.; García, R.E.; Martinez, R.F.; Martinez Calvo, M.Á. Using Genetic Algorithms with Multi-Objective Optimization to Adjust Finite Element Models of Welded Joints. *Metals* **2018**, *8*, 230. [CrossRef]
13. Busari, Y.; Manurung, Y.H.; Shuaib-Babata, Y.L.; Ahmad, S.N.; Taufek, T.; Leitner, M.; Dizon, J.R.C.; Muhammad, N.; Mohamed, M.A. Experimental validation on multi-pass weld distortion behavior of structural offshore steel HSLA S460 using FE based inherent strain and thermo-mechanical method. *MRS Commun.* **2022**, *12*, 104–111. [CrossRef]
14. Baruah, S.; Sarkar, S.; Singh, I.V.; Mishra, B.K. A computational framework based on FEA, ML and GA for estimation of welding residual stresses. *Finite Elem. Anal. Des.* **2022**, *205*, 103753. [CrossRef]
15. Teng, T.-L.; Chang, P.-H. Three-dimensional thermomechanical analysis of circumferentially welded thin-walled pipes. *Int. J. Pres. Ves. Pip.* **1998**, *75*, 237–247. [CrossRef]
16. Deng, D.; Murakawa, H. Finite element analysis of temperature field, microstructure and residual stress in multi-pass butt-welded 2.25Cr–1Mo steel pipes. *Comp. Mater. Sci.* **2008**, *43*, 681–695. [CrossRef]
17. Giri, A.; Mahapatra, M.M.; Sharma, K.; Singh, P.K. A Study on the Effect of Weld Groove Designs on Residual Stresses in SS 304LN Thick Multipass Pipe Welds. *Int. J. Steel. Struct.* **2017**, *17*, 65–75. [CrossRef]

18. Zhao, M.; Wei, F.; Huang, W.Q.; Lei, Y. Experimental and numerical investigation on combined girth welding of API X80 pipeline steel. *Sci. Technol. Weld. Join.* **2015**, *20*, 622–630. [CrossRef]
19. Wu, C.; Lee, C.; Kim, J.-W. Numerical simulation of bending deformation induced by multi-seam welding of a steel-pipe structure. *J. Mech. Sci. Technol.* **2020**, *34*, 2121–2131. [CrossRef]
20. Liu, Y.; Wang, P.; Fang, H.; Ma, N. Characteristics of welding distortion and residual stresses in thin-walled pipes by solid-shell hybrid modelling and experimental verification. *J. Manuf. Process.* **2021**, *69*, 532–544. [CrossRef]
21. Perić, M.; Garašić, I.; Tonković, Z.; Vuherer, T.; Nižetić, S.; Dedić-Jandrek, H. Numerical Prediction and Experimental Validation of Temperature and Residual Stress Distributions in Buried-Arc Welded Thick Plates. *Int. J. Energy Res.* **2019**, *43*, 3590–3600. [CrossRef]
22. Perić, M.; Nižetić, S.; Garašić, I.; Gubeljak, N.; Vuherer, T.; Tonković, Z. Numerical Calculation and Experimental Measurement of Temperatures and Welding Residual Stresses in a Thick-Walled T-Joint Structure. *J. Therm. Anal. Calorim.* **2020**, *141*, 313–322. [CrossRef]
23. Perić, M.; Nižetić, S.; Tonković, Z.; Garašić, I.; Horvat, I.; Boras, I. Numerical Simulation and Experimental Investigation of Temperature and Residual Stress Distributions in a Circular Patch Welded Structure. *Energies* **2020**, *13*, 5423. [CrossRef]
24. Sepe, R.; Giannella, V.; Greco, A.; De Luca, A. FEM Simulation and Experimental Tests on the SMAW Welding of a Dissimilar T-Joint. *Metals* **2021**, *11*, 1016. [CrossRef]
25. Deng, D.; Sun, J.; Dai, D.; Jiang, X. Influence of Accelerated Cooling Condition on Welding Thermal Cycle, Residual Stress, and Deformation in SM490A Steel ESW Joint. *J. Mater. Eng. Perform.* **2015**, *24*, 3487–3501. [CrossRef]
26. Hwang, S.-Y.; Kim, Y.; Lee, J.-H. Finite element analysis of residual stress distribution in a thick plate joined using two-pole tandem electro-gas welding. *J. Mater. Process. Technol.* **2016**, *229*, 349–360. [CrossRef]
27. Sun, J.; Liu, X.; Tong, Y.; Deng, D. A comparative study on welding temperature fields, residual stress distributions and deformations induced by laser beam welding and CO_2 gas arc welding. *Mater. Des.* **2014**, *63*, 519–530. [CrossRef]
28. Zhao, H.; Niu, W.; Zhang, B.; Lei, Y.; Kodama, M.; Ishide, K. Modelling of keyhole dynamics and porosity formation considering the adaptive keyhole shape and three-phase coupling during deep-penetration laser welding. *J. Phys. D Appl. Phys.* **2011**, *44*, 485302. [CrossRef]
29. Sisodia, R.P.S.; Gáspár, M. An Approach to Assessing S960QL Steel Welded Joints Using EBW and GMAW. *Metals* **2022**, *12*, 678. [CrossRef]
30. Baba, H.; Era, T.; Ueyama, T.; Tanaka, M. Single pass full penetration joining for heavy plate steel using high current GMA process. *Weld World* **2017**, *61*, 963–969. [CrossRef]
31. Lin, J.; Ma, N.; Lei, Y.; Murakawa, H. Measurement of residual stress in arc welded lap joints by cosα X-ray diffraction method. *J. Mater. Process. Technol.* **2017**, *243*, 387–394. [CrossRef]
32. Perić, M.; Tonković, Z.; Rodić, A.; Surjak, M.; Garašić, I.; Boras, I.; Švaić, S. Numerical Analysis and Experimental Investigation of Welding Residual Stresses and Distortions in a T-Joint Fillet Weld. *Mater. Des.* **2014**, *53*, 1052–1063. [CrossRef]
33. Deng, D.; Kiyoshima, S. Numerical simulation of welding temperature field, residual stress and deformation induced by electro slag welding. *Comp. Mater. Sci.* **2012**, *62*, 23–34. [CrossRef]
34. Perić, M.; Tonković, Z.; Karšaj, I.; Stamenković, D. A simplified engineering method for a T-joint welding simulation. *Therm. Sci.* **2018**, *22*, S867–S873. [CrossRef]
35. Trupiano, S.; Belardi, V.G.; Fanelli, P.; Gaetani, L.; Vivio, F. A novel modeling approach for multi-passes butt- welded plates. *J. Therm. Stress.* **2021**, *44*, 829–849. [CrossRef]
36. Ghafouri, M.; Ahola, A.; Ahn, J.; Björk, T. Numerical and experimental investigations on the welding residual stresses and distortions of the short fillet welds in high strength steel plates. *Eng. Struct.* **2022**, *260*, 114269. [CrossRef]
37. Deng, D. FEM Prediction of Welding Residual Stress and Distortion in Carbon Steel Considering Phase Transformation Effects. *Mater. Des.* **2009**, *30*, 359–366. [CrossRef]
38. Feng, G.; Wang, H.; Wang, Z.; Deng, D. Numerical Simulation of Residual Stress and Deformation in Wire Arc Additive Manufacturing. *Crystals* **2022**, *12*, 803. [CrossRef]
39. Wang, Y.; Feng, G.; Pu, X.; Deng, D. Influence of welding sequence on residual stress distribution and deformation in Q345 steel H-section butt-welded joint. *J. Mater. Res. Technol.* **2021**, *13*, 144–153. [CrossRef]
40. Perić, M.; Seleš, K.; Tonković, Z.; Lovrenić-Jugović, M. Numerical Simulation of Welding Distortions in Large Structures with a Simplified Engineering Approach. *Open Phys.* **2019**, *17*, 719–730. [CrossRef]
41. Perić, M.; Tonković, Z.; Maksimović, K.S.; Stamenković, D. Numerical Analysis of Residual Stresses in a T-Joint Fillet Weld Using a Submodeling Technique. *FME Trans.* **2019**, *47*, 183–189. [CrossRef]
42. Deng, D.; Murakawa, H. Numerical simulation of temperature field and residual stress in multi-pass welds in stainless steel pipe and comparison with experimental measurements. *Comp. Mater. Sci.* **2006**, *37*, 269–277. [CrossRef]